Nano Research

Open Access

Research Article

Inhalable multilevel responsive microspheres for radiation-induced lung injury

Xinlian Wang[1,2,§], Jinhui Lin[1,2,§], Dongtao Yin[3,§], Xin Li[1], Zhichen Lang[3], Guanghui Zhang[1], Yueguang Xue[1], Shilin Li[1,2], Xiao Zhang[1,2], Bing Han[3], Fengsheng Li[4], and Ying Liu[1,2] ✉

[1] *CAS Key Laboratory for Biomedical Effects of Nanomaterials and Nanosafety & CAS Center for Excellence in Nanoscience, National Center for Nanoscience and Technology of China, Beijing 100190, China*
[2] *University of Chinese Academy of Sciences, Beijing 100049, China*
[3] *Department of Cardiothoracic surgery, Rocket Force Characteristic Medical Center, Beijing 100088, China*
[4] *Rocket Force Characteristic Medical Center, Beijing 100088, China*
§ *Xinlian Wang, Jinhui Lin, and Dongtao Yin contributed equally to this work.*

Cite this article: *Nano Research*, **2025**, *18*, 94907339. https://doi.org/10.26599/NR.2025.94907339

ABSTRACT: Radiation-induced lung injury (RILI) is a severe side effect associated with radiotherapy for thoracic tumor. RILI is a complex pathological process encompassing early-stage pneumonia and late-stage pulmonary fibrosis, and the process is irreversible. Current research predominantly focuses on early-stage radiation pneumonia, while effective therapeutic approaches for pulmonary fibrosis remain lacking. Therefore, a comprehensive therapeutic strategy addressing both pneumonia and fibrosis is urgently needed for RILI. Micro-nano carriers offer new opportunities for inhalable drug delivery to the lungs, enabling efficient transport across multiple biological barriers for the treatment of pulmonary diseases. Herein, we developed an inhalable microsphere system, RP@BDC, with multilevel responsiveness, designed to meet the size requirements for pulmonary drug delivery and to intervene the entire progression of RILI. Resveratrol and siPAI-1 were chosen as therapeutic agents to inhibit inflammation and fibrosis-related proteins. Chitosan-based nanoparticles (RP@DC) were prepared to enhance drug stability and permeability. $CaCO_3$ biomineralization endowed RP@BDC with acid-responsive particle size transformation properties. RP@BDC microspheres demonstrated excellent responsiveness, releasing drug-loaded nanoparticles in response to the radiation-induced acidic environment, thereby exerting therapeutic effects. In an RILI mouse model, RP@BDC effectively alleviated both radiation-induced inflammation and pulmonary fibrosis by reducing inflammatory factors production and inhibiting plasminogen activator inhibitor 1 (PAI-1) expression. Furthermore, RP@BDC exhibited superior therapeutic efficacy compared to conventional corticosteroids drug. Overall, our multilevel responsive delivery platform offers a promising therapeutic strategy for the comprehensive treatment of RILI.

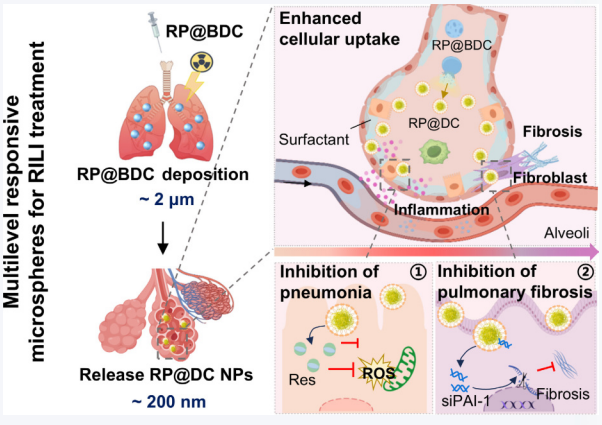

KEYWORDS: radiation-induced lung injury, microspheres, multilevel response, inhalation administration, nanoparticles

1 Introduction

As the most common type of cancer, lung cancer leads to over 1.8 million deaths globally annually [1]. Surgery, chemotherapy, and radiotherapy are the three main treatment modalities for lung cancer. For unresectable regions, radiotherapy is the preferred treatment modality. Additionally, 15%–20% of patients remain require radiotherapy due to disease progression or recurrence, making radiotherapy an irreplaceable treatment option [2]. However, radiation-induced lung injury (RILI) is a significant side effect of radiotherapy, affecting patients with lung cancer, breast cancer, or undergoing whole-body irradiation [3]. The progression of RILI includes two stages: radiation-induced pneumonia and radiation-induced pulmonary fibrosis [4]. Following ionizing radiation, lung cell damage triggers the release of inflammatory factors, leading to acute pulmonary inflammation [5]. If not

Received: December 27, 2024; **Revised:** February 15, 2025
Accepted: February 26, 2025

✉Address correspondence to liuy@nanoctr.cn

promptly intervened during this stage, the injury can progress to chronic damage, eventually develop into pulmonary fibrosis [4]. Once the pulmonary fibrosis occurs, the fibrotic process in the lungs is irreversible [5]. Therefore, preventing the occurrence and progression of RILI is particularly important. Glucocorticoids and Amifostine are commonly drugs used for the treatment of radiation-induced pneumonia, which can alleviate inflammation and reduce radiation toxicity [6, 7]. However, these treatments have serious side effects and poor tolerability. Moreover, there are no therapeutic drugs for the radiation-induced pulmonary fibrosis stage currently. Currently, most research mainly focuses on early radiation pneumonitis [8]. Therefore, there is an urgent need to develop novel treatment that can inhibit both pneumonia and pulmonary fibrosis throughout the entire progression of RILI.

Inhalation is the preferred route of administration for the treatment of pulmonary diseases. However, the pulmonary drugs delivery faces the challenge of physiological barriers in the respiratory tract that protect the lungs against the inhalation of irritants [9, 10]. The deposition of drug particles in the respiratory system exhibits the size effect. Drug particles with a diameter of 1–5 μm are easily deposited in the bronchioles and the alveoli, while particles larger than 5 μm mainly deposit in the upper respiratory tract, and particles smaller than 1 μm are easily exhaled [11, 12]. Particles smaller than 200 nm can penetrate pulmonary mucus and be internalized by alveolar cells [9, 13]. Therefore, particle size selection is a crucial consideration in inhalable drug delivery. Multi-level responsive micro and nano drug delivery systems offer new opportunities for inhalable drug delivery to the lungs, which can encapsulate drugs in biocompatible materials, enabling sustained-release treatment and reducing the frequency of administration [14–16]. Nanoparticles can be aided by micrometer-sized droplets or carriers to reach deep into the lungs, allowing for the targeted release of drugs to treat pulmonary diseases [17, 18]. The administration of hyaluronic acid nanoparticles to the lungs prior to irradiation has been shown to alleviate radiation-induced pulmonary fibrosis [19]. Poly(lactic-co-glycolic acid) (PLGA) nanoparticles encapsulating melatonin have been developed to prolong drug metabolism and provide protective effects against RILI by inhibiting the miR-21/transforming growth factor-β1 (TGF-β1) pathway [20]. However, few studies have focused on the particle size variation for optimal pulmonary drug delivery in RILI treatment.

Here, we constructed a multilevel responsive micro-nano drug delivery platform, aiming to address the particle size requirements for pulmonary drug delivery and inhibit the entire progression of RILI. As shown in Fig. 1, resveratrol (Res) and a small interfering RNA (siPAI-1) were selected as the therapeutic agents to inhibit radiation-induced inflammation and silence the expression of

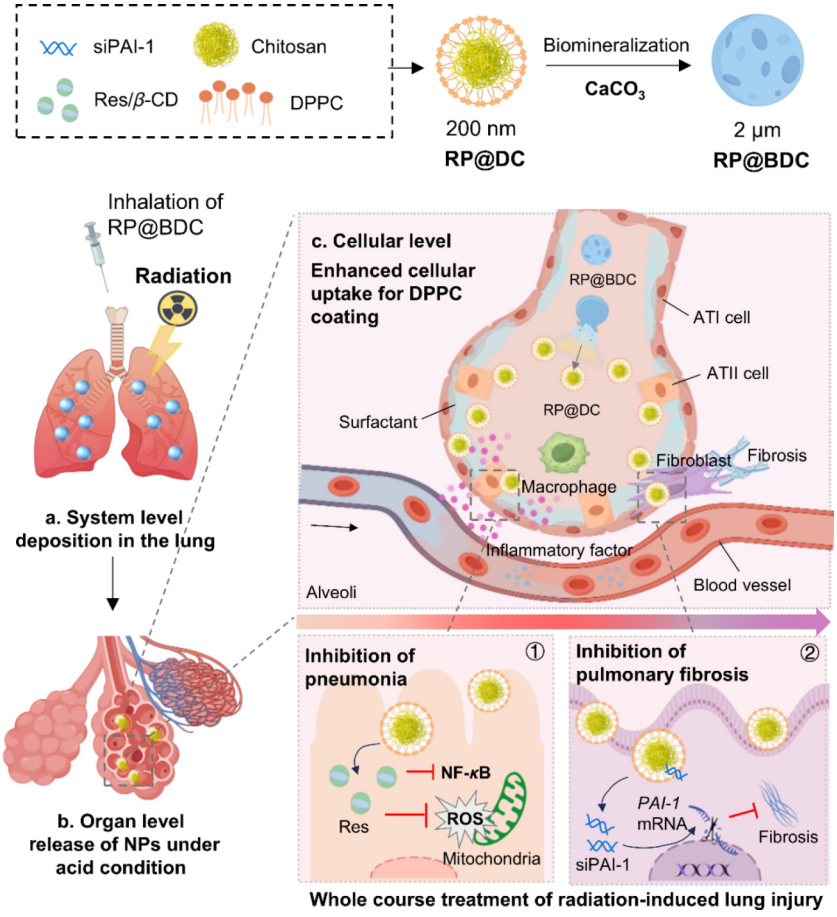

Figure 1 Schematic diagram of multilevel responsive microspheres for RILI treatment. The chitosan-based RP@DC nanoparticles loaded with an anti-inflammatory drug Res and a nucleic acid drug siPAI-1 were biomineralized into microspheres (RP@BDC). RP@BDC exhibited responsive properties at different biological levels. After inhalation, RP@BDC deposits in the deep lung and releases RP@DC nanoparticles under the radiation-induced acidic environment. RP@DC penetrates the surfactant layer and is internalized by alveoli cells, releasing Res and siPAI-1 to inhibit radiation-induced pneumonia and pulmonary fibrosis. The figure was created by Figdraw (www.figdraw.com).

fibrosis-related proteins, respectively. Chitosan coated β-cyclodextrin (β-CD) nanoparticles were prepared as nano-carriers to increase the solubility of Res and protect siRNA from degradation (RP@CS). The surface of the nanoparticles was coated with lung surfactant dipalmitoyl phosphatidylcholine (DPPC) to enhance mucus penetration (RP@DC). Moreover, RP@DC were mineralized with calcium carbonate to create a multi-level responsive microspheres (RP@BDC) with responsive properties at different biological levels. Firstly, RP@BDC can be delivered to the deep lung regions through inhalation; secondly, RP@BDC responds to the radiation-induced acidic environment to release RP@DC nanoparticles; finally, RP@DC penetrates the surfactant layer and is internalized by alveoli cells, releasing Res and siPAI-1 to inhibit pneumonia and pulmonary fibrosis. As a result, this multilevel responsive delivery platform provided a potential therapeutic strategy for the comprehensive intervention of RILI.

2 Experimental

2.1 Materials

Res and Chitosan (CS, 5 kDa) were purchased from Rhawn Reagents Co., Ltd (Shanghai, China). β-CD was purchased from lumiprobe corporation (USA). DPPC was purchased from Harveybio Co., Ltd (Beijing, China). siPAI-1 was purchased from Genepharma (Suzhou, China). Cholesterol was obtained from Innochem (Beijing, China). LipoCy5 was purchased from Flurescence (Beijing, China). Tumor necrosis factor-α (TNF-α), interleukin-1β (IL-1β) and TGF-β enzyme-Linked Immunosorbent Assay (ELISA) kits were purchased from BOSTER Biological Technology Co., Ltd (Wuhan, China). Nuclear factor kappa-B (NF-κB) ELISA kit was purchased from Shanghai Enzyme-linked Biotechnology Co., Ltd (Shanghai, China). Plasminogen activator inhibitor 1 (PAI-1) ELISA kit was purchased from Jiangsu Meimian Industrial Co., Ltd (Jiangsu, China). The sequence of siPAI-1 is as follows: Sense strand: 5'-CCAACAAGAGCCAAUCACATT-3'; Antisense strand: 5'-UGUGAUUGGCUCUUGUUGGTT-3'.

2.2 Cell lines

TC-1 mouse lung epithelial cells and mouse lung fibroblasts (PFs) were obtained from Cellverse Bioscience Technology Co., Ltd (Shanghai, China). TC-1 cells were cultured in RPMI 1640 medium (WISENT, Nanjing, China) containing 10% fetal bovine serum (FBS) (Vivacell, Germany) and 1% penicillin-streptomycin (WISENT, Nanjing, China). PFs cells were cultured in DMEM/F12 medium (WISENT, Nanjing, China) containing 10% FBS and 1% penicillin-streptomycin. Cells were cultured in a 37 °C incubator (Thermo Fisher, USA) supplemented with 5% CO_2.

2.3 Synthesis of RP@DC nanoparticles

Synthesis of β-CD-based delivery system for Res (Res/β-CD complex): β-CD was dissolved in distilled water, followed by addition of a methanol solution of Res at a 1:1 molar ratio, and stirred for 12 h at 30 °C. The resulting product Res/β-CD was obtained by lyophilization.

Synthesis of RP@CS nanoparticles: CS was dissolved in distilled water at a concentration of 33 mg/mL and stirred for 20 min in an ice bath, and then siPAI-1 aqueous solution was added at a final concentration of 3 mM and stirred for 1 h in the ice bath protected from light. Subsequently, 5 mg/mL Res/β-CD aqueous solution was added to the reaction system, followed by continuous stirring for 4 h. The resulting product RP@CS nanoparticles was obtained by lyophilization.

Synthesis of RP@DC nanoparticles: For DPPC coating, the ethanol solution containing DPPC and cholesterol was dropwise added to the aqueous dispersion of RP@CS nanoparticles. The weight ratio of DPPC, CS and cholesterol in the reaction system was 10:5:2. The reaction system was exposed to air to allow ethanol evaporate. After 4 h, the solution was passed through a 0.45 μm polycarbonate membrane using a liposome extruder, with repeated extrusion performed more than 20 times. The resulting product RP@DC nanoparticles was obtained by lyophilization.

2.4 Synthesis of RP@BDC microspheres

RP@BDC microspheres was synthesized using a template mineralization method [21]. 0.1 M $CaCl_2$ aqueous solution was added to the aqueous dispersion of RP@DC nanoparticles and stirred for 1 h. Subsequently, 0.1 M Na_2CO_3 aqueous solution was added to the reaction system and stirred for another 1 h. RP@BDC microspheres were collected by centrifugation (3000 rpm, 15 min) and then lyophilization. The only differences in the preparation processes of R@BDC and P@BDC were that the siPAI-1 and Res was not added, respectively. As for the nanoparticles loaded with fluorescent dyes (Cy5 or Cy5-siPAI-1), the fabrication method was similar to the above-described procedure for RP@BDC.

2.5 Characterization of RP@DC and RP@BDC

Particle size and surface potential of RP@DC and RP@BDC were detected by dynamic light scattering (DLS). The transmission electron microscopy (TEM) was used to detect the morphological characteristics. To assess the acid responsiveness of RP@BDC microspheres, RP@BDC was added into PBS solutions with different pH values (pH 7.4 and pH 6.2). The particle size was detected by DLS at different time points and the electron microscope samples were prepared for TEM morphology observation. For infrared spectra detection, the potassium bromide (KBr) tablet technique was used to prepare samples. The spectra of Res/β-CD, RP@DC and RP@BDC were examined using an infrared radiation exposure (IR) spectrometer (Spectrum One, Perkin Elmer Spectrum, USA) in the range of 400–4000 cm^{-1}. The drug encapsulation efficiency (EE) of Res in RP@BDC was investigated by the ultraviolet–visible (UV–Vis) absorption at 306 nm. The concentration of free Res in the supernatant was detected. Concentrations of siRNA encapsulated in RP@BDC were determined by detecting free siRNA in the supernatant using the Quant-iT RiboGreen RNA Assay kit (Thermo fisher, USA) [14]. The calculation formula of EE was shown as follows (Eq. (1)):

$$\mathrm{EE}(\%) = \frac{\text{Amount of adding drug} - \text{Amount of free drug}}{\text{Amount of adding drug}} \times 100\% \quad (1)$$

2.6 *In vitro* release behaviors of Res and siPAI-1

The release behaviors of Res and siPAI-1 from RP@BDC under different pH conditions were explored using a centrifugation method. Briefly, RP@BDC containing approximately 100 μg Res was suspended in 5 mL PBS solutions with different pH values (pH 7.4 and pH 6.2) and maintained in a shaking incubator (HX-100C, Shanghai, China) at 37 °C and 50 rpm, respectively. At scheduled

time points, 500 μL of the sample was extracted and refreshed with fresh PBS. After centrifugation at 14,000 rpm for 20 min, the collected supernatants were analyzed for Res and siPAI-1 concentration. The concentration of Res was determined using high-performance liquid chromatography (HPLC) with a UV detector at 306 nm (LC-20A, Japan). The measurement was carried out using acetonitrile/water as the mobile phase with a flow rate of 1.0 mL/min. The amount of siPAI-1 was detected by the Quant-iT RiboGreen RNA Assay kit (Thermo fisher, USA). The cumulative release of Res and siPAI-1 from RP@BDC was calculated and plotted as the release ratio over time.

2.7 *In vitro* cell cytotoxicity

The cytotoxicity of the RP@DC and RP@BDC was assessed using cell counting kit-8 (CCK-8) assays. TC-1 cells and PFs were seeded at densities of 1×10^4 cells/well in 96-well plates. Post 24 h, the cells were exposed to various concentrations of RP@DC and RP@BDC in medium. Following 24- and 48-h incubation, the supernatant was removed, and each well was treated with 10 μL of CCK-8 solution (Solarbio, Beijing, China) and 100 μL of complete medium. The plates were then incubated at 37 °C in the dark for 1–2 h, after which the absorbance of each well was measured at a wavelength of 450 nm by use of a microplate reader (BioTek, USA).

2.8 Cellular uptake assay

To examine the cellular uptake of RP@BDC, LipoCy5 was intercalated in the microspheres as the same way as that of Res. TC-1 cells (5×10^3 cells per well) were plated on a 96-well black plate and incubated 24 h with complete medium. Then, the cells were cultured with Cy5-loaded microspheres in the medium with different pH values (pH 7.4 and pH 6.2) for 24 h. Finally, the uptake efficiency of microspheres by TC-1 cells was investigated by fluorescence microplate reader (Thermo Fisher, USA).

To examine the uptake of RP@BDC by PFs, Cy5-siPAI-1 was intercalated in the microspheres as the same way as that of siPAI-1. PFs were inoculated into 35 mm culture dishes on the first day. The next day, cells were cultured with Cy5-siPAI-1@BDC in the medium with different pH values and then cultured in a 37 °C incubator. Then, the medium was removed after a 24-h incubation, before staining using Lysotracker Green pre-warmed at 37 °C, followed by culturing at 37 °C for a further 30 min. Culture medium was removed and cells were washed three times with PBS. Then cells were fixed with 4% paraformaldehyde for 10 min and subjected to nuclear staining with dihydrochloride (DAPI) (Thermo Fisher, USA). Finally, the cells were imaged using confocal macroscope (Stellaris 8, Germany).

2.9 Cell irradiation and treatment

TC-1 cells and PFs were subjected to X-ray radiation at a dose rate of 2 Gy/min and a cumulative radiation dose of 10 Gy using a biological X-ray irradiator (XCELL, KUBTEC, USA) at the Irradiation Center of the Rocket Force Characteristic Medical Center (Beijing, China).

For intracellular mitochondrial membrane potential (MMP) detection, the changes in MMP were monitored by an enhanced mitochondrial membrane potential assay kit with JC-1 (Beyotime, Shanghai, China). TC-1 cells were treated with different formulations in the complete medium with pH 6.2 after cell irradiation. After 24 h-incubation, cells were incubated with JC-1 fluorescence dye at 37 °C in the dark for 20 min. Cells were washed three times with JC-1 staining buffer. The fluorescence intensity of JC-1 monomers and JC-1 aggregates were investigated by the fluorescence microplate reader (Thermo Fisher, USA).

For intracellular superoxide anion detection, the changes in superoxide anion were monitored using a dihydroethidium probe (Beyotime, Shanghai, Beijing). Similar to the procedure described above, after 24 h-incubation of radiated TC-1 cells with different formulations, culture medium was removed and phenol red-free medium containing 10 μM dihydroethidium was added into cell culture, followed by culturing at 37 °C for 30 min. Cells were washed three times with PBS. The fluorescence intensity was investigated by the fluorescence microplate reader (Thermo Fisher, USA).

For cell viability assay, TC-1 cells were seeded in 96-well plates and treated with different formulations in the complete medium with pH 6.2 after cell irradiation. After 24 h-incubation, culture medium was removed and CCK-8 solution (Solarbio, Beijing, China) was added to each well. The plates were then incubated at 37 °C in the dark for 1–2 h, after which the absorbance of each well was measured at a wavelength of 450 nm by use of a microplate reader (BioTek, USA).

2.10 Mouse model with RILI

Male C57BL/6 mice (8–10 weeks old) were purchased from SPF Biotechnology Co., Ltd. (Beijing, China) and bred in a pathogen-free animal room. All animal experimental procedures were approved by the ethics committee of the Rocket Force Characteristic Medical Center (KY2019040). To establish a model of RILI, mice were anesthetized with tribromoethanol (0.2 mL/10 g body weight of a 1.25% solution) and exposed to whole lung irradiation at a dose rate of 2 Gy/min and a cumulative radiation dose of 20 Gy using a biological X-ray irradiator (XCELL, KUBTEC, USA) at the Irradiation Center of the Rocket Force Characteristic Medical Center (Beijing, China). During the radiation exposure, shielded lead plates were placed over the other parts of the body. Radiation-induced pneumonia mice were humanely sacrificed 1 week after irradiation and lung samples were collected for further experiments. Radiation-induced pulmonary fibrosis mice were humanely sacrificed 8 weeks after irradiation and lung samples were collected for further experiments.

2.11 Animal grouping and administration

To investigate the effects of different formulations, the mice were randomly divided into nine groups: (a) normal control (normal mice inhaled with saline); (b) negative control (radiation-induced lung injury with saline inhalation); (c) Res inhalation group; (d) siPAI-1 inhalation group; (e) R@BDC treatment group carrying only Res; (f) P@BDC treatment group carrying only siPAI-1; (g) low-dose RP@BDC treatment group, named "RP@BDC_L"; (h) high-dose RP@BDC treatment group, named "RP@BDC_H"; and (i) prednisone treatment group. Groups (a) and (b) received a single inhalation of 50 μL of saline; groups (e), (f), (g), and (i) received a single inhalation of 1.5 mg/kg; groups (c) and (d) received a single inhalation of the drug equivalent to 1.5 mg of RP@BDC; group (h) received a single inhalation of 3 mg/kg. The inhalation volume for all groups was 50 μL. Starting from the second day after X-ray radiation, inhalation administration was performed using an animal spray lung administration device (Biojane, Shanghai, China) every other day until the mice were sacrificed on day 8 for evaluation the treatment effect of pneumonia

mice. For the administration of pulmonary fibrosis treatment, inhalation administration was continued weekly until the mice were sacrificed at week 8. Each experimental group consisted of four mice.

2.12 *In vivo* biodistribution of RP@BDC

Mice were inhaled with 1 mg/kg Cy5@BDC through a spray administration device for biodistribution studies after X-ray radiation. Following 24 h of treatment, mice were sacrificed and the main organs were isolated to monitor Cy5 fluorescence signals using an *in vivo* imaging systems (IVIS) imaging system (PerkinElmer, USA).

2.13 Immunofluorescence staining

Frozen lung tissues were embedded in optimal cutting temperature (OCT) compound, followed by sectioning into thin slices. The frozen sections were then fixed with 4% paraformaldehyde for 15 min at room temperature, washed three times with PBS, and prepared for subsequent immunofluorescence staining. Slides were subjected to nuclear staining with DAPI (Thermo Fisher, USA) for 10 min at room temperature. Slides were analyzed using a digital scanning system (Pannoramic ScanII, 3DHISTECH, Hungary).

2.14 Bronchoalveolar lavage fluid (BALF) collection

Mice were anesthetized at the sixth week post-irradiation and the trachea was cannulated. BALF buffer was obtained with a 1 mL syringe loading saline by slowly injecting and aspirating three times. Then, the BALF was collected for incubation with RP@BDC to assess the acid responsiveness of RP@BDC microspheres.

2.15 Histological analysis

For the mouse model of RILI, the lung tissues were harvested and fixed in 4% paraformaldehyde for 24 h. Then the lungs were dehydrated and embedded in paraffin, followed by sectioning and staining with hematoxylin-eosin (H&E), Masson's trichrome, and picrosirius red staining.

2.16 Pulmonary function test

The experimental animals were anesthetized and intubated with a 14-gauge cannula. Pulmonary function parameters were recorded using the FlexiVent system (SCIREQ, Canada) for endpoint measurements.

2.17 Micro-computed tomography (CT) imaging

Mice were imaged at 8-week after irradiation. Mice were anesthetized using isoflurane and then were subsequently immobilized in a cradle during CT image acquisition with a single photon emission computed tomography (Triumph, USA). Scanner parameter settings: X-ray tube voltage at 90 kV; X-ray tube current at 160 μA; image projections captured during 360-degree rotation.

2.18 ELISA analysis

Lung tissues were homogenized using a tissue grinding machine (Servicebio, Wuhan, China). After centrifugation, the supernatant was stored at −80 °C for ELISA analysis. The concentration of TNF-α, IL-1β, NF-κB, TGF-β and PAI-I were estimated by ELISA Kits according to the manufacturer's instructions. Briefly, Antibodies and standard samples were diluted were added to enzyme-labeled plates and incubated for 90 min. Biotinylated antibodies were added into the plate and incubated for 60 min. Finally, HRP-linked detection antibodies were added into the plate and the absorbance at 450 and 630 nm was measured in an ELISA plate reader (BioTek, USA).

2.19 Statistical analysis

All experimental data in this study were analyzed using Graphpad Prism (v 8.0.2). Data were presented as mean ± standard deviation (SD). Statistical analyses were performed through one-way ANOVA or two-sample t-test. $^{*}P < 0.05$, $^{**}P < 0.01$, and $^{***}P < 0.001$ were deemed to indicate increasing levels of statistical significance.

3 Results and discussion

3.1 Synthesis and characterization of RP@DC and RP@BDC

The preparation process of the nanoparticles RP@DC and the microspheres RP@BDC are shown in Fig. 2(a). Under the specified pH conditions, electrostatic interactions are formed between the amino groups of chitosan and the oxygen atoms of β-CD, which facilitate the assembly of nanoparticles (RP@CS) [22, 23]. After encapsulation with DPPC, nanoparticles with a uniform particle size distribution were obtained (RP@DC), with an average diameter of 150.3 ± 3.10 nm (Fig. 2(b)), which is beneficial for the penetration of lung mucus and cellular uptake. Next, template mineralization was employed to prepare calcium carbonate ($CaCO_3$) mineralized microspheres (RP@BDC). As shown in Fig. 2(c), the average diameter of RP@BDC microspheres ranges from 2 to 3 μm, which meets the size requirements for inhalational administration and is favorable for deposition in the deep lungs. Concurrently, the Zeta potential of the RP@BDC microspheres turned from +9.24 to −16.5 mV after the mineralization (Fig. 2(d)). Further observation using TEM revealed that both RP@DC nanoparticles and RP@BDC microspheres had a uniform spherical shape (Figs. 2(e) and 2(f)).

According to the FT-IR spectra, the peak at 1418 cm^{-1} of RP@BDC microspheres corresponds to the C=O stretching vibration peak in $CaCO_3$ (Fig. 2(g)). This peak is broader and shifted compared to the peak in the standard $CaCO_3$ infrared spectrum, indicating the presence of organic matter in the product [24, 25]. Additionally, the characteristic peaks of Res at 1600 cm^{-1} for C=C stretching vibration and 1132 cm^{-1} for C–C stretching vibration were obscured in RP@BDC microspheres. These results indicated the successful encapsulation of the RP@DC nanodrug within the microspheres. The drug encapsulation efficiency was measured, with the encapsulation efficiency of RES in RP@BDC microspheres being 70.6% ± 4.6% and the encapsulation efficiency of siPAI-1 being 97.8% ± 0.14%. Collectively, micro-nano drug delivery platform was successfully constructed for pulmonary drug delivery and can effectively load both small-molecule anti-inflammatory drugs and anti-fibrotic nucleic acid drugs for RILI treatment.

3.2 Verification of multilevel responsiveness of RP@BDC

The designed RP@BDC are expected to be responsive at different structural levels (Fig. 3(a)). Firstly, during inhalation administration, RP@BDC microspheres can be deposited in the lesion site deep within the lung due to their suitable particle size. Acidic substances will be produced in the lungs when acute pneumonia occurs, due to

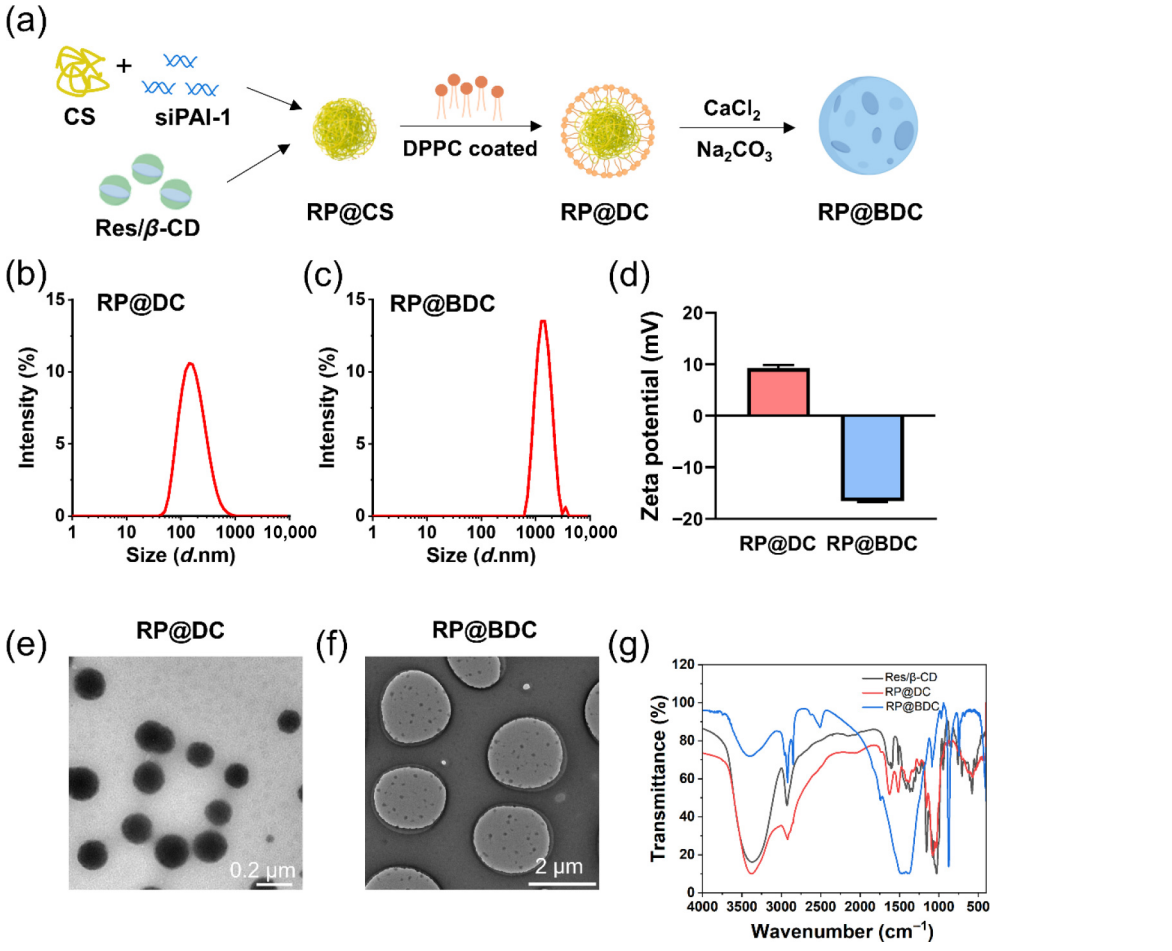

Figure 2 Preparation and characterization of RP@DC and RP@BDC. (a) The fabrication process of RP@DC and RP@BDC. Hydrodynamic size of (b) RP@DC and (c) RP@BDC. (d) Zeta potential of RP@DC and RP@BDC. TEM images of (e) RP@DC and (f) RP@BDC. (g) Infrared spectra of Res/β-CD, RP@DC and RP@BDC.

activation of the immune system and inflammatory responses, leading to an acidic microenvironment in the lungs [26]. After the RP@BDC microspheres reach the lesion site, the acidic microenvironment causes the degradation of the mineralized $CaCO_3$ shell of RP@BDC, exposing the RP@DC nanoparticles subsequently. Lastly at cellular level, RP@DC nanoparticles penetrate the mucus layer and are internalized by pulmonary epithelial cells and fibrotic cells to release the drug. To verify the pH-responsive performance of RP@BDC microspheres, RP@BDC was incubated in PBS with different pH values. The samples were collected at various time points to assess changes in their particle size. From Figs. S1(a) and S1(b) in the Electronic Supplementary Material (ESM), as the pH was decreased to 6.2, RP@BDC microspheres rapidly disintegrate from micron-sized particles to nanometer-sized particles within 30 min, releasing RP@DC nanoparticles within. In contrast, there is no significant change in particle size within 30 min under pH 7.4, with only minor surface wear.

The multilevel responsiveness of RP@BDC was further evaluated at these three levels. At system level, we replaced the internal drug with the fluorescent material Cy5 to investigate the *in vivo* distribution of RP@BDC. After 24 h of inhalation administration, RP@BDC predominantly deposited in the lungs, with no distribution in other organs (Fig. 3(b)), suggesting that inhalation administration can effectively target the lungs while reducing the distribution of the drug in other organs. Moreover, compared with normal mice, RP@BDC can rapidly degrade and release Cy5 nanoparticles in the lungs of RILI mice (one week post irradiation), in response to radiation-induced acidic environment. In contrast, although RP@BDC deposited in the deep lung of normal mice, it cannot effectively degrade and release the Cy5 nanoparticles, resulting in a local distribution in the normal lungs.

At organ level, the acid-responsive release performance of RP@BDC was further verified by immunofluorescence staining. After 24 h of inhaled administration, most of the micron-sized particles indicated by the arrows had not completely degraded (Fig. 3(c)). The fluorescence distribution of Cy5 nanoparticles is mostly on the surface of the alveolar trachea, with less nanoparticles entering the deep alveoli. In contrast, no undegraded micron-sized particles was observed in the RILI lungs after 24 h of inhalation administration and the released Cy5 nanoparticles were evenly distributed throughout the lungs. RP@BDC was further incubated with BALF of RILI mice (Fig. 3(d)). Consistently, RP@BDC microspheres degraded in the radiation-induced acidic physiological environment, releasing the nanoparticles that remained monodispersed without aggregation, and the particle sizes was similar to those of RP@DC. In addition, we also observed the dynamic size changes of RP@BDC in the BALF of RILI mice (Fig. S1(c) in the ESM). RP@BDC microspheres rapidly degraded into nanometer-sized particles within only 10 min and maintained a stable particle size of around 200 nm within 60 min without aggregation. Interestingly, RP@BDC disintegrate more rapidly in

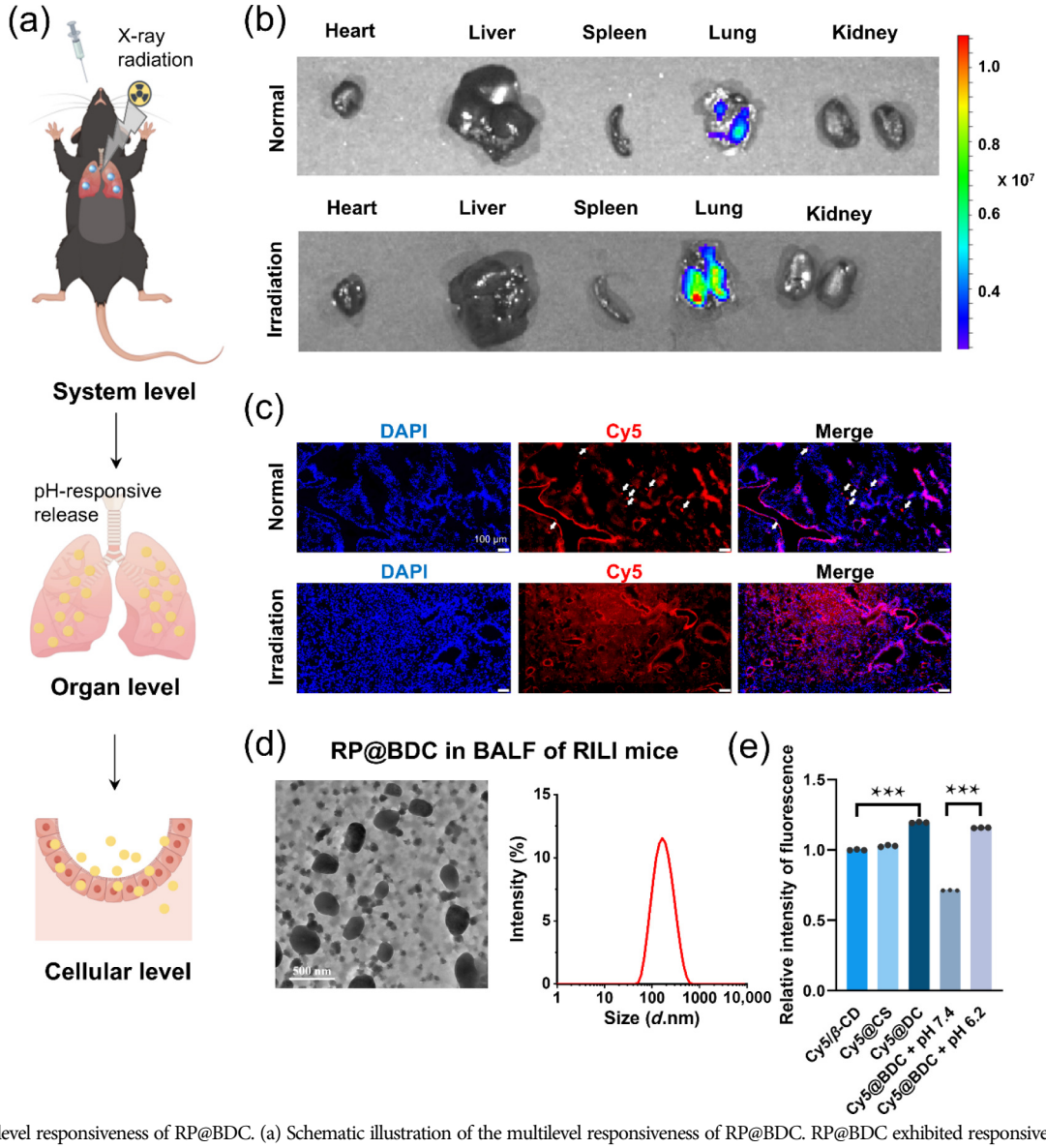

Figure 3 Multilevel responsiveness of RP@BDC. (a) Schematic illustration of the multilevel responsiveness of RP@BDC. RP@BDC exhibited responsiveness at different biological levels including the system level, organ level and cellular level. The figure was created by Figdraw. (www.figdraw.com). (b) Images of various organs at 24 h after RP@BDC inhalation in normal mice and RILI mice. (c) Representative images of immunostaining for Cy5@BDC in lung tissues of normal mice and RILI mice. Scale bars: 100 μm. (d) TEM image and size distribution of RP@BDC in BALF of RILI mice for 30 min. (e) Internalization of Cy5@BDC in TC-1 cells under different pH value conditions, analyzed by relative fluorescence intensity of Cy5. Data are presented as mean ± SD (n = 3). The P values were calculated using one-way ANOVA test. ***P < 0.001.

acidic BALF than in acidic PBS. This may due to the presence of more bioactive substances in the BALF, which facilitates the degradation of the $CaCO_3$ microsphere shell. The effective release of the internal nanodrugs is a key feature of responsive micro-nano carriers [27, 28]. Moreover, the Res and siPAI-1 release profiles from RP@BDC were monitored. As shown in Figs. S1(d) and S1(e) in the ESM, more than 60% of Res was released from RP@BDC after 24 h under the acidic condition of pH 6.2, which was approximately 5-fold higher than that observed at pH 7.4. Similarly, the accumulative release of siPAI-1 was less than 20% even after 72 h under the pH 7.4 condition, whereas it was increased to approximately 80% at pH 6.2 after 72 h. These data suggested that RP@BDC could rapidly degrade, exposing the internal RP@DC nanoparticles and effectively release the drug under acidic conditions, which is essential for subsequent therapeutic efficacy.

Subsequently at cellular level, the cellular uptake capacity of RP@DC nanoparticles was evaluated. DPPC, a major component of pulmonary surfactant, plays a critical role in reducing alveolar surface tension, thereby facilitating alveolar expansion and maintaining normal respiratory function [29]. Therefore, the encapsulation of DPPC assists drug delivery to the lungs and cellular uptake. Moreover, DPPC contributes to repair and regeneration processes in cases of lung injury [30]. To evaluate the cellular uptake efficiency of nanoparticles, Cy5 as a fluorescent probe was encapsulated into our DPPC nanoparticles. As shown in Fig. 3(e), the uptake of DPPC-coating nanoparticle (Cy5@DC) by lung epithelial cells was significantly higher than that of Cy5/β-CD and Cy5/CS nanoparticles without DPPC. Notably, for Cy5@BDC microspheres, the internal Cy5@DC nanoparticles cannot be released from the mineralized microspheres under neutral

conditions, resulting in reduced cellular uptake. While under acidic conditions, Cy5@DC were effectively released from the microspheres, leading to significantly increased cellular uptake, suggesting the pH-responsive cellular uptake capability of RP@BDC. The efficient cellular uptake of RP@BDC prolongs drug retention in the lungs, supporting sustained therapeutic effects and enhancing anti-inflammatory and antifibrotic efficacy *in vivo*. Collectively, these results demonstrate that RP@BDC microspheres exhibit specific responsiveness across biological levels, from the system level to the cellular level, making them a promising drug delivery platform for RILI treatment.

3.3 RP@BDC reduces radiation-induced cell damage

The biocompatibility of RP@DC nanoparticles and RP@BDC microspheres *in vitro* was assessed via the CCK-8 assay in the lung epithelial cells (TC-1) and PF. No significant decrease of cell viability was observed in RP@DC or RP@BDC treated cells (Figs. S2(a) and S2(b) in the ESM), suggesting that our delivery platform exhibits good biocompatibility *in vitro*. To identify the underlying effect of RP@BDC on radiation-induced cell damage, the TC-1 cell lines were subjected to attain a dose of 10 Gy X-ray radiation (Fig. 4(a)). As shown in Fig. 4(b), IR significantly decreased the mitochondrial potential, analyzed by the cationic JC-1 probe [31]. While the addition of RP@DC and RP@BDC was able to restore the mitochondrial membrane potential under acidic conditions. Superoxide anion, a major type of reactive oxygen species (ROS), is produced by the single-electron reduction of molecular oxygen. Continuously increasing oxidative stress caused by radiation leads to the generation of large amounts of ROS, which ultimately results in DNA damage and cellular death [8]. After RP@BDC treatment, the level of superoxide anion was significantly alleviated compared with that of the IR group (Fig. 4(c)). Finally, CCK-8 assay was utilized to evaluate the effect of RP@BDC on cell viability 24 h after irradiation. RP@BDC significantly increased the viability of cells,

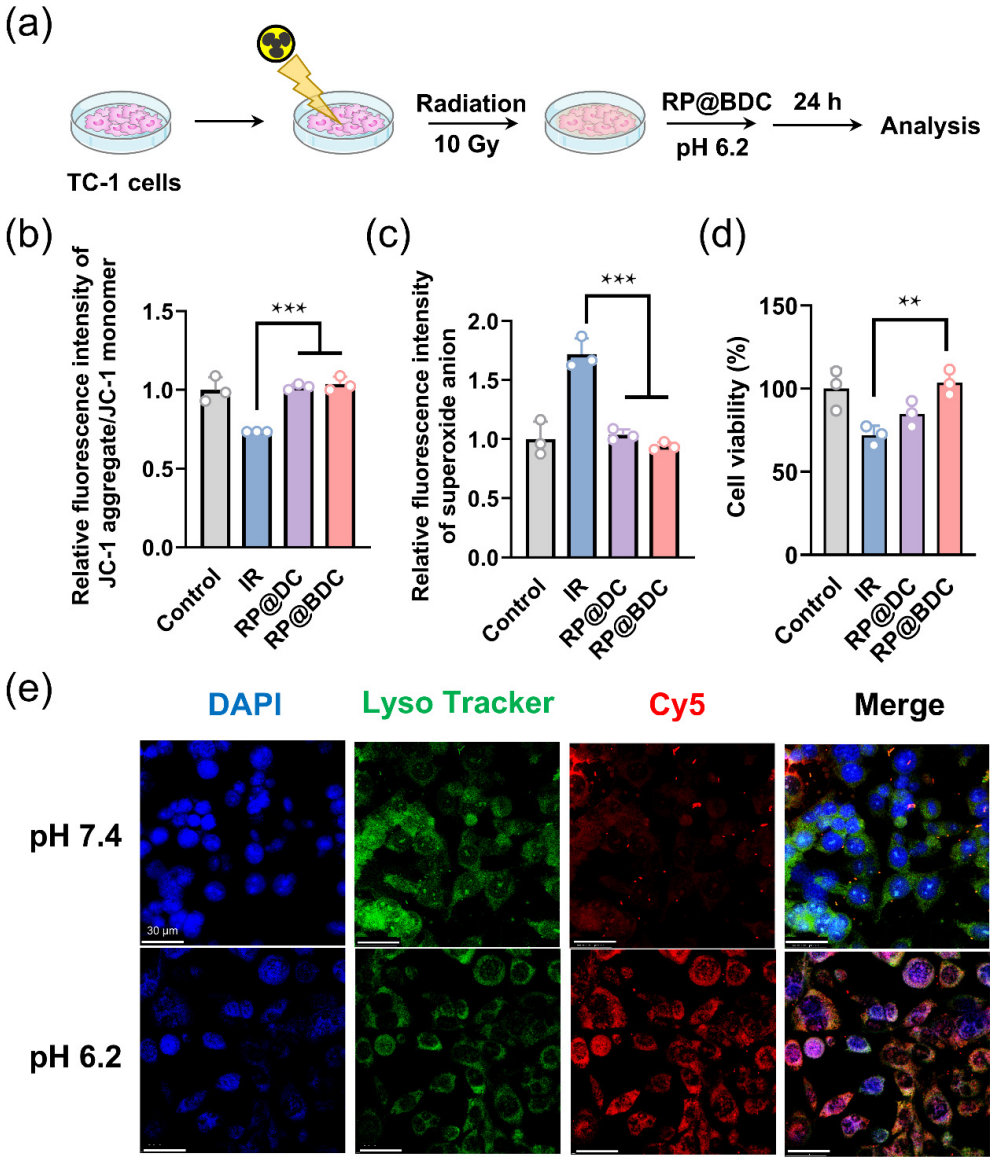

Figure 4 RP@BDC reduces radiation-induced cell damage. (a) Diagram illustrating the irradiation process for TC-1 cells. (b) Relative fluorescence intensity ratio of JC-1 aggregates to monomers. (c) Relative fluorescence intensity of superoxide anion. (d) The effect of RP@BDC on the viability of TC-1 cells induced by IR. (e) Cy5-siPAI-1@BDC uptake in PFs observed by confocal microscopy at 24 h. Scale bars: 30 μm. Data are presented as mean ± SD (n = 3). The P values were calculated using one-way ANOVA test. $^{**}P < 0.01$, $^{***}P < 0.001$.

effectively alleviating radiation-induced cell damage (Fig. 4(d)). These data suggested that RP@BDC can be internalized by TC-1 cells under acidic conditions and release the drug resveratrol, inhibiting the radiation-induced oxidative stress and reducing cell damage. Oxidative stress is a key pathological process in radiation-induced lung injury, triggering inflammation and fibrosis [4]. By alleviating oxidative stress, RP@BDC helps to reduce further lung tissue damage, thereby enhancing lung function. The reduction in cell damage also contributes to the protection of alveolar structure and function, which is expected to decrease radiation-induced inflammation and fibrosis in the lungs.

The responsive release and cellular uptake capabilities of RP@BDC in fibroblasts were also evaluated. PF cells were exposed to Cy5-siPAI-1@BDC under different pH conditions and intracellular distribution of the microspheres was analyzed. Under acidic conditions, the $CaCO_3$ shell was degraded and Cy5-siPAI-1@DC nanoparticles were released, resulting in an enhanced Cy5 fluorescence intensity (Fig. 4(e)). While under neutral conditions, the microspheres failed to release the internal nanoparticles and could not be internalized by the cells. In summary, RP@BDC can be effectively internalized by lung epithelial cells and fibroblasts, demonstrating radiation-induced antioxidative stress effects and good biocompatibility. This suggests that RP@BDC may have beneficial effects against radiation-induced pneumonia and pulmonary fibrosis. Overall, the *in vitro* results lay the foundation for the therapeutic potential of RP@BDC in RILI, prompting us to further investigation into its *in vivo* efficacy in animal models.

3.4 Inhalable RP@BDC alleviates radiation-induced pneumonia

After confirming the effects of RP@BDC on protecting epithelial cells against radiation-induced cellular damage *in vitro*, we proceeded to verify their therapeutic effects on an RILI model. Radiation-induced pneumonia mice were established by X-ray radiation with 20 Gy to the whole thorax and then treated by inhalation of RP@BDC for 7 days (Fig. 5(a)). Here we established single-drug-loaded groups (R@BDC and P@BDC), a low-dose dual-drug-loaded group (RP@BDC_L), and a high-dose dual-drug-loaded group (RP@BDC_H). Moreover, the glucocorticoid drug prednisone was selected as a positive control to evaluate the therapeutic efficacy of our RP@BDC microspheres. As shown in H&E staining, the tracheal and alveolar wall epithelial cells are clear in normal mice (Fig. 5(b)). While in irradiated mice, the trachea and epithelial cells exhibited inflammation-induced swelling and dilation, accompanied by thickened alveolar walls. Similar structural features were observed in the free RES group, siPAI-1 group, and P@BDC (only encapsulating siPAI-1) group. Conversely, the alveolar structure in the lungs of mice in the R@BDC group, RP@BDC_L, and RP@BDC_H group were basically normal, with only a small number of regions showing alveolar wall congestion and thickening, which were similar to the prednisone group. These results indicated that inhaled Res-loaded microspheres can effectively alleviate radiation-induced pneumonia in mice.

TNF-α and IL-1β are two key proinflammatory cytokines that play important roles in immune responses and inflammatory processes. TNF-α and IL-1β significantly increase after irradiation, which will promote the cascade reaction of cytokines and accelerate the fibroblast proliferation and interstitial cell infiltration [32, 33]. The relative concentrations of TNF-α and IL-1β in the lungs of mice in different groups were measured, with the concentrations in the negative control lungs taken as a relative value of 1 (Fig. 5(c)). The levels of both TNF-α and IL-1β in the lungs significantly increased after radiation exposure. Interestingly, inhalation of Res-loaded microspheres significantly reduced the production of TNF-α and IL-1β in a dose-dependent manner. High-dose RP@BDC group showed the most significant inhibitory effect on the expression of inflammatory factors, reducing their levels to those comparable to the normal group. Res exhibits anti-inflammatory effect via suppressing NF-κB activation [34]. To further explore the therapeutic mechanisms, the expression of NF-κB in the lungs was examined. Consistently, the expressions of NF-κB were significantly suppressed after treatment with R@BDC and RP@BDC (Fig. 5(c)). Overall, our results showed that RP@BDC can effectively alleviate radiation-induced inflammatory response in the lungs, contributing to alleviating the pneumonitis symptoms at the early stage of RILI.

Patients who receive high-dose radiotherapy to the lung have been shown to experience a decline in pulmonary function, resulting in symptoms such as shortness of breath and wheezing [35]. Therefore, pulmonary function is a critical indicator for the treatment of RILI. Across our series of pulmonary function tests, inhaled RP@BDC microspheres demonstrated a dose-dependent improvement in lung function. Notably, the high-dose RP@BDC treatment group significantly mitigated radiation-induced pulmonary dysfunction, including improvements in static airway resistance (Rrs), respiratory system elastance (Ers), and lung compliance (Crs) (Fig. 5(d)). Radiation-induced cellular damage leads to structural disruption of the alveoli, which in turn impairs gas exchange and lung mechanical function, resulting in decreased lung function. The improvement in lung function further supports the protective effects of RP@BDC. These *in vivo* results are consistent with our *in vitro* findings, where RP@BDC treatment was shown to reduce cellular damage (Fig. 4(d)). H&E staining of other major organs showed no obvious abnormalities after administration of microspheres (Fig. S3 in the ESM), indicating the favorable biosafety of RP@BDC. Our results suggested that RP@BDC has good potential for reducing radiation-induced pneumonia and improving pulmonary function of radiotherapy patients.

3.5 Inhalable RP@BDC alleviates radiation-induced pulmonary fibrosis

Radiation-induced pulmonary fibrosis is the late stage of RILI. Persistent oxidative stress and inflammatory responses lead to the overactivation of lung fibroblasts, resulting in collagen deposition and the initiation of pulmonary fibrosis [4, 36]. It is essential to focus on the comprehensive treatment of RILI; however, most studies focus primarily on the early-stage intervention for pneumonia. After confirming the alleviating effect of RP@BDC on pneumonia, we next evaluated their therapeutic effects on radiation-induced pulmonary fibrosis over a longer duration (Fig. 6(a)). At the eighth week post-radiation, H&E staining showed thickened lung stroma and disrupted alveolar structure in the negative control group (Fig. S4(a) in the ESM). Similar changes were observed in free Res, free siPAI-1 and prednisone groups. This suggests that prednisone could only alleviate the early-stage pneumonia, but its effect on late-stage pulmonary fibrosis was limited. In contrast, RP@BDC treatment at both low and high doses strongly mitigated the severity of the radiation-induced fibrosis by preserving alveolar epithelial structures. Masson and picrosirius red staining demonstrated a substantial reduction in collagen deposition and

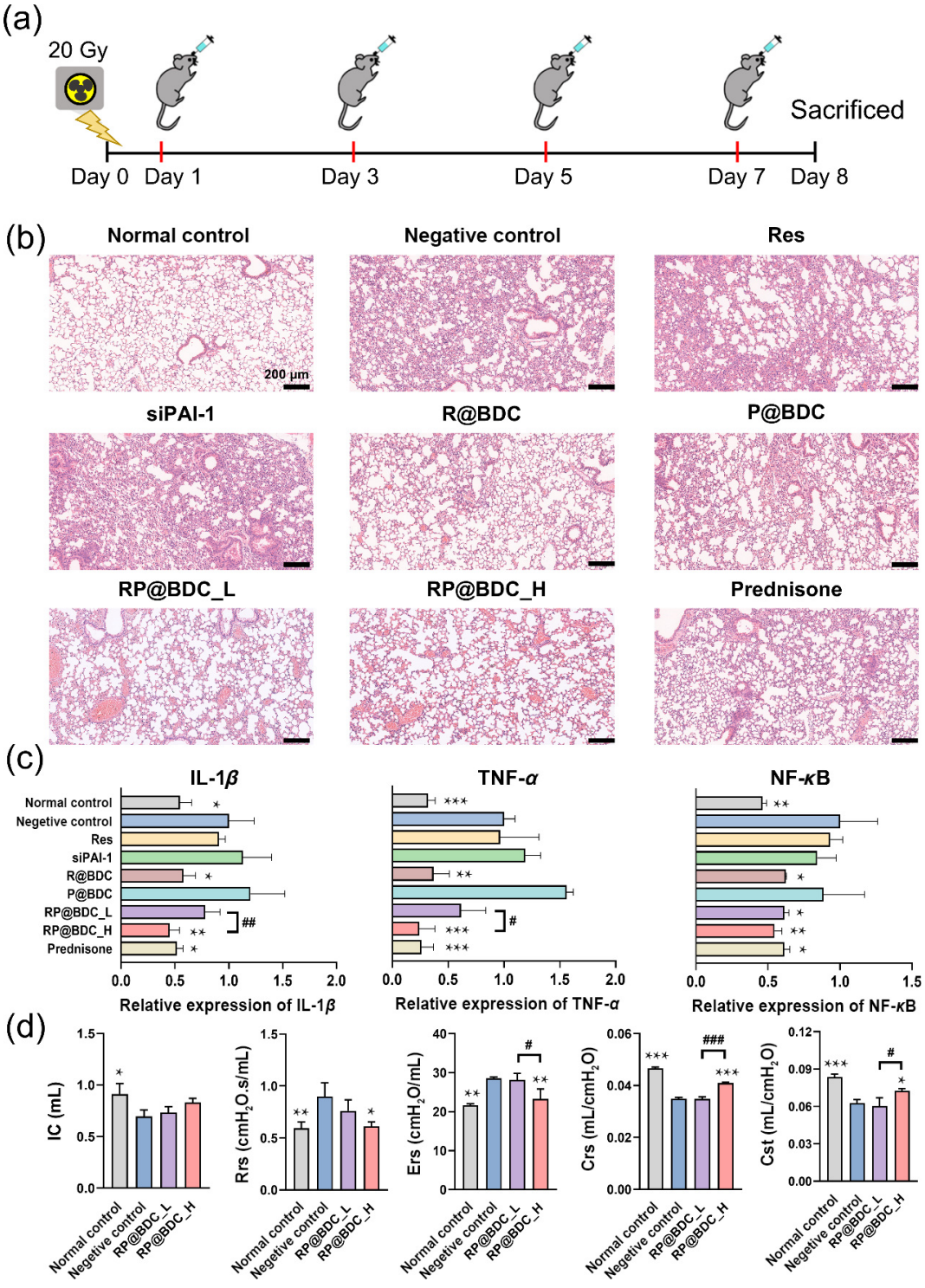

Figure 5 Inhalable RP@BDC alleviates radiation-induced pneumonia. (a) Schematic timeline of radiation-induced mice with pneumonia. (b) Representative images of lung tissue section stained with H&E. Scale bars: 200 μm. (c) Relative contents of IL-1β , TNF-α and NF-κB in the lungs of mice with radiation pneumonia (n = 4). The concentrations in the negative control lungs taken as a relative value of 1. (d) Pulmonary function effects of different formulations on lung function parameters (n = 3). Cst: static lung compliance. Data are presented as mean ± SD. The P values were calculated using one-way ANOVA test or two-sample t-test. *P < 0.05, **P < 0.01, ***P < 0.001 vs. Negative Control . $^{\#}P$ < 0.05, $^{\#\#}P$ < 0.01 between RP@BDC_L and RP@BDC_H groups.

parenchymal disruption after inhalation of RP@BDC microspheres compared to other groups (Fig. 6(b), and Fig. S4(b) in the ESM), indicating that our inhalation delivery platform can effectively inhibit lung fibrosis. Furthermore, CT imaging revealed a reduction in lung parenchymal density in RP@BDC-treated mice, with no obvious ground-glass opacities observed compared to other groups (Fig. S5 in the ESM).

PAI-1 has been identified as a critical factor in the development and progression of pulmonary fibrosis [37]. The level of PAI-1 has been shown to be significantly elevated in fibrotic tissues, which

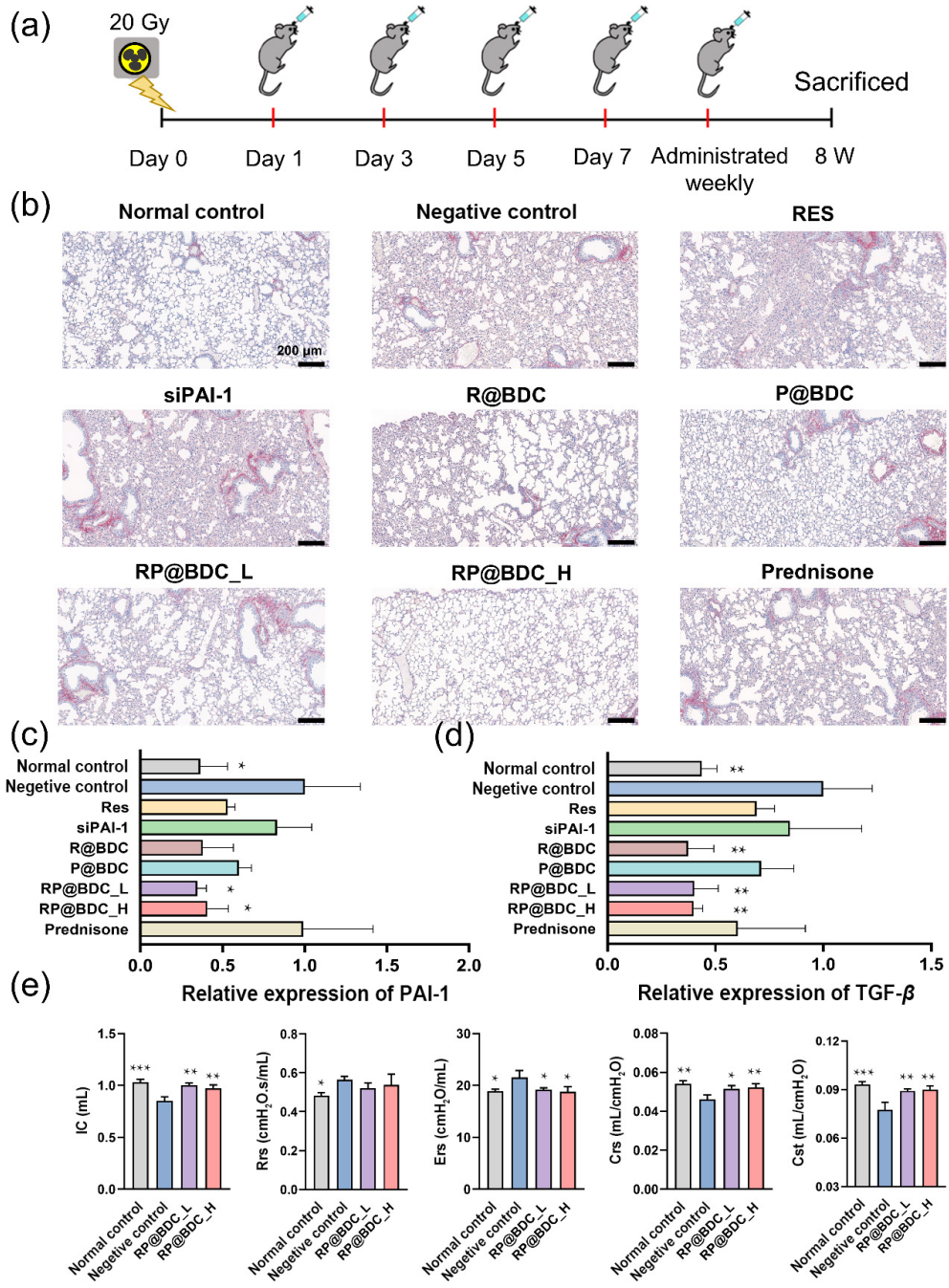

Figure 6 Inhalable RP@BDC alleviates radiation-induced pulmonary fibrosis. (a) Schematic timeline of radiation-induced mice with pulmonary fibrosis. (b) Representative images of lung tissue section stained with picrosirius red. Scale bars: 200 μm. Relative contents of (c) PAI-1 and (d) TGF-β in the lungs of mice with radiation-induced pulmonary fibrosis (n = 4). The concentrations in the negative control lungs taken as a relative value of 1. (e) Pulmonary function effects of different formulations on lung function parameters (n = 3). Data are presented as mean ± SD. The P values were calculated using one-way ANOVA test. *P < 0.05, **P < 0.01, ***P < 0.001.

blocks fibrinolysis and promote collagen accumulation, contributing to the progression of fibrosis [38]. In our experiment, the expression level of PAI-1 in the lungs of negative control mice was significantly elevated at the eighth week post-radiation (Fig. 6(c)). Inhalation of RP@BDC at both low and high doses significantly reduced the PAI-1 expression, indicating the effectiveness of our siRNA delivery platform. Fibrosis is consistently marked by increased TGF-β expression. Fibroblasts activation in response to TGF-β leads to increased nuclear sizes and extracellular matrix protein expression [39]. RP@BDC treatment significantly inhibited TGF-β expression in RILI mice (Fig. 6(d)). Notably, our results suggest that the treatment of radiation-induced pulmonary fibrosis requires simultaneous suppression of both pneumonia and fibrosis. Single-agent siPAI-1 treatment was ineffective in alleviating pulmonary fibrosis, highlighting the crucial role of early inflammation control in mitigating radiation-induced fibrosis. This also emphasizes the importance of combination therapy in RILI treatment. Single-agent therapies can only target specific pathways to alleviate localized symptoms, whereas RILI involves multiple complex processes. Combining anti-inflammatory and anti-fibrotic

drugs provides a more comprehensive approach to addressing the entire progression from early inflammation to pulmonary fibrosis.

The pulmonary function of fibrosis mice was also evaluated after the administration of RP@BDC (Fig. 6(e)). Inhalation of RP@BDC showed a trend toward improving pulmonary function including inspiratory capacity (IC), Ers and Crs in fibrosis mice. Meanwhile, H&E staining of other major organs showed no obvious abnormalities after 8-week administration of microspheres (Fig. S6 in the ESM), demonstrating a great biocompatibility of RP@BDC for a long-term administration. Glucocorticoids are the current clinical treatment for pneumonia. However, oral or intravenous administration of glucocorticoids have been reported to cause severe side effects, including hyperglycemia, osteoporosis, and hepatotoxicity [40–42]. Our inhalable RP@BDC drug delivery system enables localized drug release in the lungs, minimizing systemic exposure and potential side effects. Even after 8 weeks of prolonged administration, no significant toxicity was observed. Moreover, glucocorticoids primarily suppress inflammation but do not directly address fibrosis progression. In contrast, RP@BDC combines both anti-inflammatory and anti-fibrotic effects, demonstrating better therapeutic efficacy in RILI treatment.

4 Conclusions

In summary, we fabricated a multilevel responsive microsphere for the comprehensive treatment of RILI, including the early-stage pneumonia and late-stage fibrosis. RP@BDC microspheres demonstrated excellent response performance across various biological levels ranging from the systemic to the cellular level, releasing the drug-loaded nanoparticles in response to the radiation-induced acidic environment, thereby exerting their therapeutic effects. Corticosteroids, such as prednisone, are currently effective drugs for treating pneumonia; however, they are unable to inhibit the progression of pulmonary fibrosis. In our study, the combination therapy of the anti-inflammatory drug Res and the anti-fibrosis nucleic acid drug siPAI-1 effectively alleviated radiation-indued pneumonia and pulmonary fibrosis, showing greater efficacy than monotherapy. Our multilevel responsive delivery platform provides a potential inhalation therapeutic approach for the comprehensive intervention of RILI.

Electronic Supplementary Material: Supplementary material (*in vitro* characterization of acid responsiveness of RP@BDC; biocompatibility of RP@BDC *in vitro* and *in vivo*; histological analysis of RP@BDC for RILI treatment; lung CT scans of RP@BDC for RILI treatment) is available in the online version of this article at https://doi.org/10.26599/NR.2025.94907339.

Data availability

All data needed to support the conclusions in the paper are presented in the manuscript and the Electronic Supplementary Material. Additional data related to the findings of this study are available from the corresponding author upon reasonable request.

Acknowledgements

This work was supported by the National Nature Science Foundation of China (Nos. 22476031, 22388101, and 22027810). We extend our thanks to Jiao Mu from Institute of Chemistry, Chinese Academy of Sciences for the imaging by confocal microscope. We also thank Figdraw (www.figdraw.com) for the assistance in creating Figs. 1 and 3(a).

Declaration of competing interest

All the contributing authors report no conflict of interests in this work.

Author contribution statement

All authors have contributions to this work. X. L. W. and J. H. L.: Experimental design, data collection and analysis, and writing manuscript. J. H. L, D. T. Y, and F. S. L: Construction of the animal model. X. L., X. Z., and Z. C. L.: Contributors to part of the animal experiments. G. H. Z and Y. G. X: Contributors to part of the cell experiments. S. L. L. and B. H.: Contributors to part of the synthesis and characterization of nanoparticles. Y. L.: Responsible for supervising the study and reviewing the manuscript.

Informed consent

Not applicable.

Ethics statement

The animal experiments were carried out following the guidelines of the Ethics Committee of the Rocket Force Characteristic Medical Center for the Care and Use of Laboratory Animals and were approved by the Ethics Committee of the Rocket Force Characteristic Medical Center (Ethical code: KY2019040).

Use of AI statement

None.

References

[1] Jokhadze, N.; Das, A.; Dizon, D. S. Global cancer statistics: A healthy population relies on population health. *CA Cancer J. Clin.* **2024**, *74*, 224–226.

[2] Woodman, C.; Vundu, G.; George, A.; Wilson, C. M. Applications and strategies in nanodiagnosis and nanotherapy in lung cancer. *Semin. Cancer Biol.* **2021**, *69*, 349–364.

[3] Giuranno, L.; Ient, J.; De Ruysscher, D.; Vooijs, M. A. Radiation-induced lung injury (RILI). *Front. Oncol.* **2019**, *9*, 877.

[4] Hanania, A. N.; Mainwaring, W.; Ghebre, Y. T.; Hanania, N. A.; Ludwig, M. Radiation-induced lung injury: Assessment and management. *Chest* **2019**, *156*, 150–162.

[5] Roy, S.; Salerno, K. E.; Citrin, D. E. Biology of radiation-induced lung injury. *Semin. Radiat. Oncol.* **2021**, *31*, 155–161.

[6] Obrador, E.; Salvador, R.; Villaescusa, J. I.; Soriano, J. M.; Estrela, J. M.; Montoro, A. Radioprotection and radiomitigation: From the bench to clinical practice. *Biomedicines* **2020**, *8*, 461.

[7] Rhen, T.; Cidlowski, J. A. Antiinflammatory action of glucocorticoids-new mechanisms for old drugs. *N. Engl. J. Med.* **2005**, *353*, 1711–1723.

[8] Zhang, Y. L.; Huang, J. F.; Li, S. P.; Jiang, J. L.; Sun, J. J.; Chen, D.; Pang, Q. F.; Wu, Y. X. Pyrroloquinoline quinone alleviates mitochondria damage in radiation-induced lung injury in a MOTS-c-dependent manner. *J. Agric. Food Chem.* **2024**, *72*, 20944–20958.

[9] Yue, L. D.; Zhang, X. Y.; Zhao, C. C.; Chen, R. C.; Chen, X. Y.; Rao, L. Inhaled drug delivery: Past, present, and future. *Nano Today* **2023**, *52*, 101942.

[10] Wang, X. L.; Gao, X. L.; Wang, L. X.; Lin, J. H.; Liu, Y. Advances of

nanotechnology toward vaccine development against animal infectious diseases. *Adv. Funct. Mater.* **2023**, *33*, 2305061.
[11] Kumbhar, P.; Manjappa, A.; Shah, R.; Jha, N. K.; Singh, S. K.; Dua, K.; Disouza, J.; Patravale, V. Inhalation delivery of repurposed drugs for lung cancer: Approaches, benefits and challenges. *J. Control. Release* **2022**, *341*, 1–15.
[12] Guo, Y.; Bera, H.; Shi, C. Z.; Zhang, L.; Cun, D.; Yang, M. S. Pharmaceutical strategies to extend pulmonary exposure of inhaled medicines. *Acta Pharm. Sin. B* **2021**, *11*, 2565–2584.
[13] Murgia, X.; Pawelzyk, P.; Schaefer, U. F.; Wagner, C.; Willenbacher, N.; Lehr, C. M. Size-limited penetration of nanoparticles into porcine respiratory mucus after aerosol deposition. *Biomacromolecules* **2016**, *17*, 1536–1542.
[14] Wang, L. X.; Xue, Y. G.; Wang, X. L.; Pan, Y.; Li, S. L.; Mei, J.; Jiang, S. S.; Zheng, Q.; Liu, Y.; Liu, Y. et al. DEPDC1 is a potential therapeutic target in lung adenocarcinoma. *Nano Today* **2024**, *56*, 102249.
[15] Hu, M. D.; Li, X. Y.; You, Z.; Cai, R.; Chen, C. Y. Physiological barriers and strategies of lipid-based nanoparticles for nucleic acid drug delivery. *Adv. Mater.* **2024**, *36*, 2303266.
[16] Zhang, G. F.; Cong, Y. L.; Liu, F. L.; Sun, J. F.; Zhang, J. T.; Cao, G. L.; Zhou, L. Q.; Yang, W. J.; Song, Q. L.; Wang, F. J. et al. A nanomaterial targeting the spike protein captures SARS-CoV-2 variants and promotes viral elimination. *Nat. Nanotechnol.* **2022**, *17*, 993–1003.
[17] Ye, T.; Jiao, Z. G.; Li, X.; He, Z. L.; Li, Y. Y.; Yang, F. M.; Zhao, X.; Wang, Y. C.; Huang, W. J.; Qin, M. et al. Inhaled SARS-CoV-2 vaccine for single-dose dry powder aerosol immunization. *Nature* **2023**, *624*, 630–638.
[18] Xiong, L. S.; Li, X. Y.; Lu, X. J.; Zhang, Z. D.; Zhang, Y.; Wu, W.; Wang, C. H. Inhaled multilevel size-tunable, charge-reversible and mucus-traversing composite microspheres as Trojan horse: Enhancing lung deposition and tumor penetration. *Chin. Chem. Lett.* **2024**, *35*, 109384.
[19] Lierova, A.; Kasparova, J.; Pejchal, J.; Kubelkova, K.; Jelicova, M.; Palarcik, J.; Korecka, L.; Bilkova, Z.; Sinkorova, Z. Attenuation of radiation-induced lung injury by hyaluronic acid nanoparticles. *Front Pharmacol.* **2020**, *11*, 1199.
[20] Wang, S.; Li, J.; He, Y. J.; Ran, Y. H.; Lu, B. H.; Gao, J. N.; Shu, C.; Li, J.; Zhao, Y. Z.; Zhang, X. et al. Protective effect of melatonin entrapped PLGA nanoparticles on radiation-induced lung injury through the miR-21/TGF-β1/Smad3 pathway. *Int. J. Pharm.* **2021**, *602*, 120584.
[21] Lee, C. H.; Jin, E. S.; Lee, J. H.; Hwang, E. T. Immobilization and stabilization of enzyme in biomineralized calcium carbonate microspheres. *Front. Bioeng. Biotechnol.* **2020**, *8*, 553591.
[22] Wang, H. X.; Hu, L. D.; Peng, L.; Du, J.; Lan, M. C.; Cheng, Y.; Ma, L.; Zhang, Y. H. Dual encapsulation of β-carotene by β-cyclodextrin and chitosan for 3D printing application. *Food Chem.* **2022**, *378*, 132088.
[23] Jiang, Y. Z.; Liu, B. C.; Xu, J. K.; Pan, K. L.; Hou, H. J.; Hu, J. P.; Yang, J. K. Cross-linked chitosan/β-cyclodextrin composite for selective removal of methyl orange: Adsorption performance and mechanism. *Carbohydr. Polym.* **2018**, *182*, 106–114.
[24] Zapata, P. A.; Palza, H.; Díaz, B.; Armijo, A.; Sepúlveda, F.; Ortiz, J. A.; Ramírez, M. P.; Oyarzún, C. Effect of $CaCO_3$ nanoparticles on the mechanical and photo-degradation properties of LDPE. *Molecules* **2018**, *24*, 126.
[25] Shen, Q.; Wei, H.; Zhou, Y.; Huang, Y. P.; Yang, H. R.; Wang, D. J.; Xu, D. F. Properties of amorphous calcium carbonate and the template action of vaterite spheres. *J. Phys. Chem. B* **2006**, *110*, 2994–3000.
[26] Zhang, C. Y.; Lin, W. J.; Gao, J.; Shi, X. T.; Davaritouchaee, M.; Nielsen, A. E.; Mancini, R. J.; Wang, Z. J. pH-responsive nanoparticles targeted to lungs for improved therapy of acute lung inflammation/injury. *ACS Appl. Mater. Interfaces* **2019**, *11*, 16380–16390.
[27] Chen, X.; Wang, L. L.; Zhang, J. T.; Yan, H. Y.; Wang, S. H.; Xiao, J. X. Controlled release of ceria and ferric oxide nanoparticles via collagen hydrogel for enhanced osteoarthritis therapy. *Adv. Healthc. Mater.* **2024**, *13*, 2401507.
[28] Wang, L. Y.; Shi, Y. Y.; Jiang, J. Z.; Li, C.; Zhang, H. R.; Zhang, X. H.; Jiang, T.; Wang, L.; Wang, Y. Y.; Feng, L. Micro-nanocarriers based drug delivery technology for blood-brain barrier crossing and brain tumor targeting therapy. *Small* **2022**, *18*, 2203678.
[29] Liao, R.; Sun, Z. C.; Wang, L. Y.; Xian, C. H.; Lin, R.; Zhuo, G. F.; Wang, H. Y.; Fang, Y. F.; Liu, Y. T.; Yang, R. Y. et al. Inhalable and bioactive lipid-nanomedicine based on bergapten for targeted acute lung injury therapy via orchestrating macrophage polarization. *Bioact. Mater.* **2025**, *43*, 406–422.
[30] Yu, Z. C.; Liu, X. Y.; Chen, H. J.; Zhu, L. F. Naringenin-loaded dipalmitoylphosphatidylcholine phytosome dry powders for inhaled treatment of acute lung injury. *J. Aerosol Med. Pulm. Drug Deliv.* **2020**, *33*, 194–204.
[31] Sivandzade, F.; Bhalerao, A.; Cucullo, L. Analysis of the mitochondrial membrane potential using the cationic JC-1 dye as a sensitive fluorescent probe. *Bio. Protoc.* **2019**, *9*, e3128.
[32] Liu, X. L.; Shao, C. L.; Fu, J. M. Promising biomarkers of radiation-induced lung injury: A review. *Biomedicines* **2021**, *9*, 1181.
[33] Malaviya, R.; Laskin, J. D.; Businaro, R.; Laskin, D. L. Targeting tumor necrosis factor alpha to mitigate lung injury induced by mustard vesicants and radiation. *Disaster Med. Public Health Prep.* **2023**, *17*, e553.
[34] Ren, Z. H.; Wang, L.; Cui, J. H.; Huoc, Z.; Xue, J. R.; Cui, H.; Mao, Q. Q.; Yang, R. R. Resveratrol inhibits NF-κB signaling through suppression of p65 and IκB kinase activities. *Pharmazie* **2013**, *68*, 689–694.
[35] Niezink, A. G. H.; de Jong, R. A.; Muijs, C. T.; Langendijk, J. A.; Widder, J. Pulmonary function changes after radiotherapy for lung or esophageal cancer: A systematic review focusing on dose-volume parameters. *Oncologist* **2017**, *22*, 1257–1264.
[36] Seto, Y.; Kaneko, Y.; Mouri, T.; Shimizu, D.; Morimoto, Y.; Tokuda, S.; Iwasaku, M.; Yamada, T.; Takayama, K. Changes in serum transforming growth factor-beta concentration as a predictive factor for radiation-induced lung injury onset in radiotherapy-treated patients with locally advanced lung cancer. *Transl. Lung Cancer Res.* **2022**, *11*, 1823–1834.
[37] Shioya, S.; Masuda, T.; Senoo, T.; Horimasu, Y.; Miyamoto, S.; Nakashima, T.; Iwamoto, H.; Fujitaka, K.; Hamada, H.; Hattori, N. Plasminogen activator inhibitor-1 serves an important role in radiation-induced pulmonary fibrosis. *Exp. Ther. Med.* **2018**, *16*, 3070–3076.
[38] Loskutoff, D. J.; Quigley, J. P. PAI-1, fibrosis, and the elusive provisional fibrin matrix. *J. Clin. Invest.* **2000**, *106*, 1441–1443.
[39] Budi, E. H.; Schaub, J. R.; Decaris, M.; Turner, S.; Derynck, R. TGF-β as a driver of fibrosis: Physiological roles and therapeutic opportunities. *J. Pathol.* **2021**, *254*, 358–373.
[40] Cho, J. H.; Suh, S. Glucocorticoid-induced hyperglycemia: A neglected problem. *Endocrinol. Metab* **2024**, *39*, 222–238.
[41] Kimura, H.; Takeda, A.; Kikukawa, T.; Hasegawa, I.; Mino, T.; Uchida-Kobayashi, S.; Ohsawa, M.; Itoh, Y. Liver injury after methylprednisolone pulse therapy in multiple sclerosis is usually due to idiosyncratic drug-induced toxicity rather than autoimmune hepatitis. *Mult. Scler. Relat. Disord.* **2020**, *42*, 102065.
[42] Fu, W. Y.; Chen, M.; Wang, K. D.; Chen, Y. J. N.; Cui, Y. Z.; Xie, Y. L.; Lei, Z. N.; Hu, W. H.; Sun, G. D.; Huang, G. W. et al. Tau is a receptor with low affinity for glucocorticoids and is required for glucocorticoid-induced bone loss. *Cell Res.* **2025**, *35*, 23–44.